



Article

Performance of Mg/Al and Zn/Al Hydroxide Double Lamellar-Bentonite for Removal of Anionic Azo Dye from Aqueous Solution

Mohammed Mustapha Bouhent ¹, Kahina Bentaleb ^{2,3}, Abdulrahman Al-Ameri ^{2,3}  and Ulrich Maschke ^{3,*} 

- ¹ Laboratoire de l'Ingénierie des Procédés de l'Environnement (LIPE), Université des Sciences et de la Technologie d'Oran Mohamed Boudiaf (USTOMB), BP 1505, El M'naouer, Oran 31000, Algeria
- ² Laboratoire Physico-Chimie des Matériaux-Catalyse et Environnement (LPCMCE), Université des Sciences et de la Technologie d'Oran Mohamed Boudiaf (USTOMB), BP 1505, El M'naouer, Oran 31000, Algeria
- ³ Unité Matériaux et Transformations (UMET), UMR 8207, Univ. Lille, CNRS, INRAE, Centrale Lille, F-59000 Lille, France
- * Correspondence: ulrich.maschke@univ-lille.fr

Abstract: This paper presents the preparation and characterization of bentonite coated with hydroxide double lamellar Mg/Al-bentonite and Zn/Al-bentonite as a potential adsorbent material. The coating process involved co-precipitation of mixed metal nitrate solution (Mg-Al) or (Zn-Al), followed by immersion of bentonite (B-Na⁺) dispersion. The structures and morphologies of the coated bentonites were characterized using XRD, FTIR, BET, and SEM analysis. The results of the BET analysis indicate that Mg/Al-bentonite and Zn/Al-bentonite have larger surface areas and pore volumes compared to bentonite alone. Specifically, the surface area of Mg/Al-bentonite is 209.25 m²/g with a pore volume of 0.423 cm³/g, while Zn/Al-bentonite has a surface area of 175.95 m²/g and a pore volume of 0.313 cm³/g. In contrast, the surface area and pore volume of bentonite alone are 110.43 m²/g and 0.132 cm³/g, respectively. The Mg/Al-bentonite reaches 85% uptake within 3 h (equivalent to 724.20 mg/g at 25 °C and pH 7), achieving rapid equilibrium. In contrast, the Zn/Al-bentonite achieves a maximum adsorption of 74% within 5 h under identical pH and temperature conditions, corresponding to 650.34 mg/g. The error function values, including the correlation coefficient R^2 , chi-square test χ^2 , and residual sum of squares RSS, were calculated to evaluate both kinetic and isotherm models. The kinetic adsorption data agreed well with a pseudo-second-order model. The adsorption process followed the Sips isotherm model, and the monolayer adsorption capacity of Mg/Al-bent and Zn/Al-bent composites was 872.41 ($R^2 = 0.974$) and 678.45 mg/g ($R^2 = 0.983$), respectively. The thermodynamic analysis of the adsorption process revealed that it occurred spontaneously with an endothermic characteristic. The parameters ΔS , ΔH , and ΔG were used to determine this.



Citation: Bouhent, M.M.; Bentaleb, K.; Al-Ameri, A.; Maschke, U. Performance of Mg/Al and Zn/Al Hydroxide Double Lamellar-Bentonite for Removal of Anionic Azo Dye from Aqueous Solution. *Processes* **2024**, *12*, 677. <https://doi.org/10.3390/pr12040677>

Academic Editors: Marwa El-Azazy, Saeed Al-Meer, Ahmed El-Shafie and Khalid Al-Saad

Received: 26 January 2024

Revised: 19 March 2024

Accepted: 21 March 2024

Published: 28 March 2024



Copyright: © 2024 by the authors. Licensee MDPI, Basel, Switzerland. This article is an open access article distributed under the terms and conditions of the Creative Commons Attribution (CC BY) license (<https://creativecommons.org/licenses/by/4.0/>).

Keywords: wastewater treatment; azoic orange II dye; adsorption; bentonite; layered double hydroxides

1. Introduction

Dyes are organic products that are extensively applied in the textile industry and are released at relatively high concentrations in effluents. They contribute to the toxicity of water and pose a growing danger to the environment, humans, and animals [1]. Azo dyes are the largest category of dyes, representing 60–70% of all dyes used for industrial purposes. Currently, there are more than 2000 azo dyes available on the market for dyeing various materials, including wool, leather, viscose, silk, synthetic fibers, and cotton. They are also used in plastic, paints, rubber, and varnishes.

The European Commission has supported several initiatives to evaluate the risks associated with azo colorants. Certain azo dyes have been classified as carcinogens, which is why their use is restricted in the EU. Simultaneously, assessments were conducted to analyze the socio-economic impacts in Europe and the rest of the world that could

result from these restrictions. It should be noted that a considerable quantity of azo dyes is released as wastewater, resulting in persistent environmental impacts. The removal of dyes from wastewater is a significant environmental concern. Dyes have complex aromatic molecular structures that make them stable and resistant to biodegradation. Previous studies have shown that biological methods can effectively eliminate azo dyes from aqueous solutions [2–4].

Currently, there are several methods employed to eliminate dyes from industrial wastewater [5–8]. Of these, adsorption is a highly effective technique for removing a broad spectrum of dyes. The selection of an adsorbent should be based on characteristics such as robust affinity, the ability to target specific compounds, and the feasibility of regenerating the adsorbent [9–12].

Activated carbons are commonly used as adsorbents due to their high adsorption capacities. However, activated carbon is relatively expensive, so many reports have considered other substitutes [13]. Clay minerals are gaining recognition for their potential use as environmental remediation agents [14,15]. Due to its cost-effectiveness, wide availability, and the high specific surface area provided by its sheet-like structure, bentonite is a commonly used adsorbent. Bentonite is a commonly used clay mineral [16,17], composed mainly of montmorillonite, which is a type of clay recognized as a 2/1 type aluminosilicate. Its crystalline arrangement is characterized by octahedral alumina between two tetrahedral silica layers. The clay has a negative surface charge due to the substitution of Al^{3+} for Si^{4+} in the tetrahedral layer and Mg^{2+} for Al^{3+} in the octahedral layer. Exchangeable cations, typically Na^+ and Ca^{2+} , neutralize the negative charges on the surface and counterbalance this charge imbalance [18]. Although bentonite has a significant capacity for adsorbing cationic dyes [19–21], it often struggles to effectively remove anionic dyes.

Because wastewater containing various pollutants has both positively and negatively charged elements, it is crucial to create a customized adsorbent that can efficiently remove both types of charges. To accomplish this, clay minerals have been modified to produce a modified form of bentonite by introducing molecules, compounds, and organic/inorganic complexes. These modifications increase their adsorption capacity for anionic organic compounds. Several research investigations have explored modifying and characterizing bentonite by intercalating hydroxyls or oxides in the basal spacing to enhance its adsorption capabilities for anionic dyes. Hao et al. (2019) conducted a study on the adsorption of dyes, including acid turquoise blue A (ATBA), basic green (BG), and basic fuchsin (BF), by hydroxyaluminum-pillared bentonite [22]. Chinoune and colleagues developed a magnesium hydroxide-coated bentonite for the efficient removal of anionic reactive dyestuffs, in particular Remazolbrilliant blue R (RB) and Procion blue HP (PB), from aqueous media [23]. Desai et al. developed chromium-metal polycations intercalated with bentonite as adsorbents with varying chromium content using an economical and sustainable method. These adsorbents were used to remove two different dyes: cationic Basic Orange II and anionic Acid Blue 74 [24].

Composite development has been used to enhance bentonite performance for specific applications by incorporating materials with different properties [25,26]. Synergistic combinations of low-cost adsorbents, such as anionic and cationic clays, are gaining attention [27,28]. Anionic clays significantly modify the charge of bentonite, also known as layered double hydroxides (LDH). Anionic clays are hydroxides of metals that have positively charged layers. These layers have a general formula of $[M_{1-x}^{II} M_x^{III}(\text{OH})_2]^{x+} (A^{n-})_{\frac{x}{n}} m\text{H}_2\text{O}$ where M^{III} and M^{II} represent trivalent and divalent metal cations, respectively. A^{n-} corresponds to hydrated interlayer regions that balance the layers' positive charges. x is given by the ratio of $M^{III}/(M^{III} + M^{II})$ [29]. For the removal of the anionic dye Eriochrome Black T (EBT), Mu'azu et al. prepared a composite of bentonite and LDH as an adsorbent using the co-precipitation technique. The prepared sample demonstrated a superior affinity for EBT adsorption. As a result, the EBT adsorption capacity was significantly increased from 361.01 mg/g of the starting material to 675.67 mg/g [30]. By heterocoagulation of LDH colloids and delaminated bentonite, Hu et al. developed an adsorbent for the removal of the

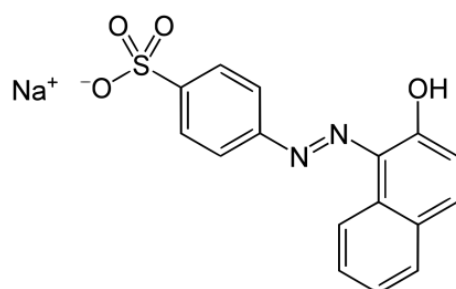
anionic dye Reactive Yellow 2 (RY2). According to the research, intercalating bentonite with a Mg-Al-Cl LDH greatly enhances its ability to adsorb RY2, increasing it from negligible to nearly 100% [31].

The adsorption of Orange II on LDH-coated bentonite has not been reported to our knowledge. Our previous experiments have demonstrated that LDHs are highly effective adsorbents for the azoic dye Orange II.

2. Materials and Methods

2.1. Materials

Acid Orange 7, also known as Orange II and identified by CAS number 633-96-5, is an azo dye that was acquired from Sigma-Aldrich, located in Steinheim, Germany. The adsorbent did not need to be purified prior to use. Scheme 1 shows the chemical structure of Orange II.



Scheme 1. Chemical structure of Orange II dye.

The bentonite utilized in this study was purchased from the ENOF company (El Harrach, Algiers, Algeria) and contains approximately 80% montmorillonite with the following structural formula: $(\text{Si}_{7.41}\text{Al}_{0.59})^{\text{IV}}(\text{Al}_{2.82}\text{Fe}_{0.24}\text{Mg}_{0.48})^{\text{VI}}(\text{Ca}_{0.08}\text{Na}_{0.76}\text{K}_{0.1})\text{O}_{20}(\text{OH})_2$, as previously reported [32]. The cation exchange capacity of the bentonite was 101.25 meq/g, measured by the methylene blue method [33]. To facilitate composite synthesis, the original bentonite was purified and transformed into B- Na^+ by treatment with a 1 M NaCl solution (Sigma-Aldrich, Steinheim, Germany), following the procedure described in [18].

$\text{MgCl}_2 \cdot 5\text{H}_2\text{O}$, $\text{ZnCl}_2 \cdot 5\text{H}_2\text{O}$, $\text{Al}(\text{NO}_3)_3 \cdot 9\text{H}_2\text{O}$, and NaOH were used without purification from Acros Organics (Geel, Belgium) with a purity of at least 99% for $\text{MgCl}_2 \cdot 5\text{H}_2\text{O}$ and $\text{ZnCl}_2 \cdot 5\text{H}_2\text{O}$, 99% for $\text{Al}(\text{NO}_3)_3 \cdot 9\text{H}_2\text{O}$, and >97% for NaOH.

2.2. Preparation of Coated Bentonite Composite

The coating procedure was conducted using co-precipitation, as shown in Figure 1. First, a suspension of 1 g B- Na^+ in 100 cm³ of distilled water was stirred for 48 h at room temperature. This allowed the interlayer cations to hydrate and the lamellae to expand. Then, a 50 mL metal solution was carefully added to this suspension. To prepare the Mg/Al-bentonite (named Mg/Al-bent) and Zn/Al-bentonite (named Zn/Al-bent) composites, two solutions were prepared, one containing 1.743 g of $\text{Mg}(\text{NO}_3)_2 \cdot 6\text{H}_2\text{O}$ and 1.275 g of $\text{Al}(\text{NO}_3)_3 \cdot 9\text{H}_2\text{O}$, and the second containing 2.022 g of $\text{Zn}(\text{NO}_3)_2 \cdot 6\text{H}_2\text{O}$ and 1.275 g of $\text{Al}(\text{NO}_3)_3 \cdot 9\text{H}_2\text{O}$, which were added to the clay suspension. The aim was to achieve a stoichiometric ratio of $M^{\text{II}}/M^{\text{III}} = 2$ and a total metal concentration of 1 mol/L (refer to Figure 1). Concurrently, a 0.5 M NaOH solution was added drop-by-drop. The alkaline solution was carefully regulated to maintain a constant pH of 10 for ($\text{Mg}^{2+} + \text{Al}^{3+}$) and a pH of 8 for ($\text{Zn}^{2+} + \text{Al}^{3+}$). The process was conducted under a nitrogen atmosphere. This minimized contamination from atmospheric CO_2 . The solution was stirred vigorously and allowed to age at room temperature for a period of 12 h. The precipitate was then filtered, washed with distilled water until no NO_3^- was detected, and dried at 30 °C.

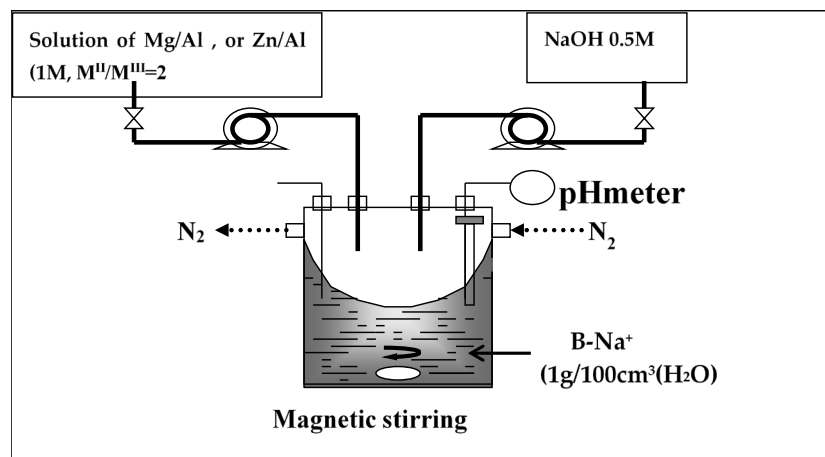


Figure 1. Experimental setup for the synthesis of coated bentonite.

2.3. Characterizations

The powder X-ray diffraction patterns of Mg/Al-bent and Zn/Al-bent were obtained using a Siemens D-5000 diffractometer (Bruker, Karlsruhe, Germany) with monochromatic $\text{CuK}\alpha$ radiation ($\lambda = 1.5418 \text{ \AA}$) at 30 mA and 40 kV. The scanning rate was $4^\circ/\text{min}$, and the 2θ angle varied from 5° to 60° . FTIR analysis was performed with a PHILIPS PU 9714 spectrophotometer (Philips, Amsterdam, The Netherlands) using the KBr pellet technique.

To avoid diffusion effects, the sample was finely ground. Under vacuum at room temperature, a mixture of 99 mg of pure KBr and 1 mg of the sample was compressed. A Micromeritics ASAP 2460 adsorption apparatus (Micromeritics, Norcross, GA, USA) was used to perform N_2 adsorption and desorption studies at 77 K. The Brunauer–Emmett–Teller (BET) method was used to calculate the specific surface area. For scanning electron microscope (SEM) studies, the adsorbent samples were positioned on the SEM grid. A sputter coater (SPI Supplies, West Chester, PA, USA) was used to deposit a thin gold layer on the samples at 30 mA for 2 min. The characterization of the samples was performed with a scanning electron microscope (SEM), model Joel JSM-5910, Jeol, Tokyo, Japan. The SEM was operated under full vacuum. The accelerating voltage was 8 kV.

2.4. Adsorption Experiments

The batch technique was used to conduct adsorption experiments and investigate the effects of adsorbent dosage, initial dye concentration, solution temperature, and contact time. Stock solutions were prepared by dissolving an appropriate amount of dye in distilled water to a concentration of 6 g/L Orange II, then diluting to the desired concentrations. The experiments were performed at a pH of 7. The amount of Orange II adsorbed per unit mass of Mg/Al-bent and Zn/Al-bent composites and the percentage of adsorption efficiency were calculated using Equations (1) and (2).

$$qe = (C_0 - C_e) \frac{V}{m} \quad (1)$$

$$P(\%) = 100(C_0 - C_e)/C_0 \quad (2)$$

where C_e (mg/L) and C_0 (mg/L) correspond to the equilibrium and initial Orange II concentrations, respectively; m (g) stands for the mass of the coated bentonite; and the volume of the dye solution is represented by V (L).

Control experiments were conducted under the same experimental conditions, but without the adsorbent, to assess the natural removal of the pollutant.

3. Results

3.1. Characterization of LDH

3.1.1. XRD Analysis

The confirmation of the crystallinity of the obtained LDH composites was established by comparing the diffraction peaks with those of the original bentonite, as shown in the results of the powder XRD studies. Figure 2 shows the diffractograms of the original bentonite B-Na⁺ and the synthesized Mg/Al-bent and Zn/Al-bent composites. In all cases, the diffraction patterns show typical features of layered structures. The XRD pattern of B-Na⁺ shows all the reflections of a typical dioctahedral smectite [34]. The appearance of a more intense line at $2\theta = 7.16^\circ$ and two others at $2\theta = 19.96^\circ$ and $2\theta = 28.76^\circ$ indicates that the bentonite is composed mainly of montmorillonite. These XRD patterns correlate well with the standard JCPDS file (card no. 13-0135) [23]. The distance between the layers, known as the basal spacing d_{001} and calculated from the position of the first basal reflection, was determined to be 12.47 Å.

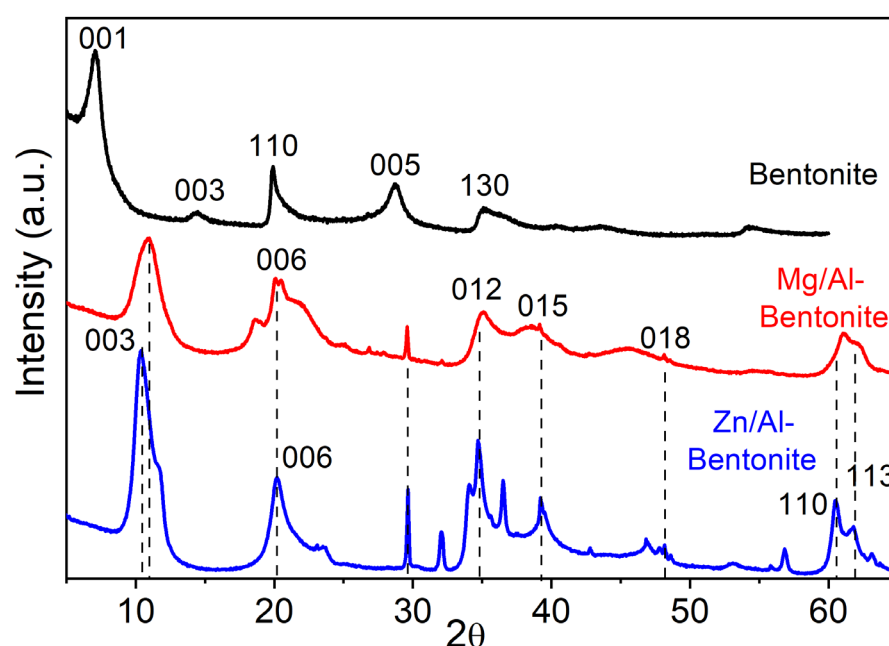


Figure 2. XRD patterns of bentonite and the synthetic LDH-bentonite composites.

Two potential explanations may clarify the absence of the distinctive (001) line of bentonite in the diffractograms of Mg/Al-bent and Zn/Al-bent composites: either the exfoliation of the lattice distance during synthesis or insufficient clay quantity added, as suggested by Kaur et al. in the fabrication of MgFe₂O₄-bentonite nanocomposites [35]. This absence is due to the fact that the cationic hydrates are fully intercalated in the interlayer space of the bentonite. As the clay was kept in water for 48 h under agitation, it is probable that the lattice distance of the clay significantly expanded. The clay content of the LDHs is more prevalent than that of the bentonite. This is supported by the emergence of new, strong, and symmetrical peaks at low 2θ values of 10.97° , 23.10° , 32.083° , and 39.26° , which are attributed to the diffraction of basal planes (003), (006), (012), and (015), respectively. Less intense peaks are observed at $2\theta = 60.56^\circ$ and 61.80° , which are generally asymmetric at higher angular values for planes (110) and (113), respectively. These results are consistent with the layered structure of LDHs. Additionally, it is evident that the (006) peak appears as a doublet peak character, indicating that after modification, the synthetic composite comprises both bentonite and LDH structures. The observations suggest that the bentonite underwent structural delamination and that the Mg/Al and Zn/Al layers were incorporated into the bentonite layers rather than simply covering the surface. Characteristic hydroxalite-type diffraction peaks were observed in the composite structure.

3.1.2. Analysis by Infrared Spectroscopy

Fourier transform infrared spectroscopy (FTIR) is a spectral technique that captures changes in the vibrational and rotational states of molecular bonds. It provides valuable insights into the presence of absorbed water molecules and structural hydroxyl groups within clay minerals, making it an exceptional tool for discerning the composition of organic compounds and mineral structures. Figure 3 shows the FTIR spectra of different composites, including Mg/Al-bent, Zn/Al-bent, and bentonite (B-Na⁺) as a reference. The spectra display similar features across all bands. The bentonite spectrum exhibits broad absorption bands that correspond to the characteristic absorption profile of montmorillonite minerals [36]. At 3628 cm⁻¹, an absorption band is attributed to the stretching vibrations of O-H groups (ν_{OH}), indicating the presence of hydroxyl groups within the silicate framework linked to octahedral cations (Al-OH-Al). A shoulder is observed around 3447 cm⁻¹, attributed to the stretching vibration of H-O-H in water molecules within the interfoliar space.

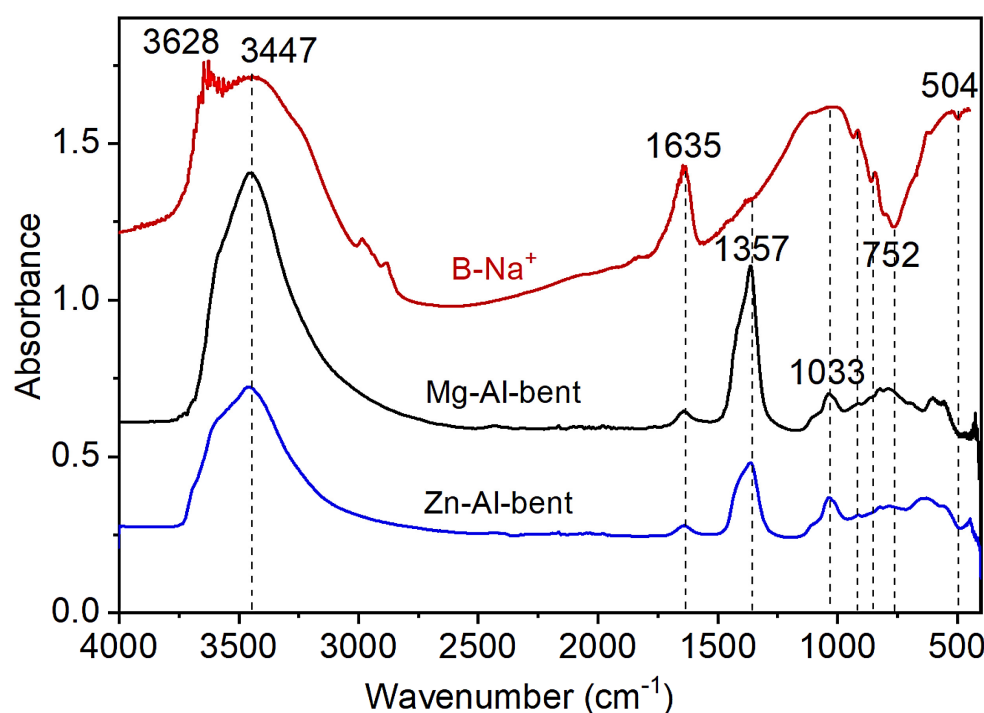


Figure 3. FTIR spectra of B-Na⁺, Mg/Al-bent, and Zn/Al-bent.

Additionally, the angular deformation of water molecules ($\delta(\text{H-O-H})$) between layers appears at 1635 cm⁻¹ [37]. Furthermore, bands in the 400–600 cm⁻¹ range indicate angular deformation in Si-O-M (M = Al, Mg, Fe, Li) bonds within layered silicates. Additionally, bands between 900 and 1000 cm⁻¹ signify metal-oxygen M-O and O-M-O vibrations [38]. The IR analysis reveals modifications in bentonite, highlighted by the emergence of a novel peak at 1357 cm⁻¹. This peak corresponds to a bond between nitro compounds and LDH bentonite [39], providing evidence for the intercalation of LDH within the layers of bentonite. It also affects Si-O vibrations in the 1200–950 cm⁻¹ region. The intense peaks at 1033 cm⁻¹ are assigned to the carbonate mode, showing that the LDH phase intercalated contains some CO₃²⁻. The peaks observed at 523, 463, and 671 cm⁻¹ are attributed to the deformation of Si-O-Al, Si-O-Mg, and Si-O-Si, respectively. The 981 cm⁻¹ band corresponds to the valence vibrations of the Si-O bond in the plane. The redistribution of the OH group among Fe, Mg, and Al atoms in octahedral positions can induce frequency shifts in vibrations (δ Al-Al-OH, δ Al-Fe-OH, and δ Al-Mg-OH) to lower values, approximately 935, 861, and 814 cm⁻¹.

3.1.3. Analysis by BET

Figure 4 displays the nitrogen adsorption–desorption isotherms of B- Na^+ , Zn/Al-bent, and Mg/Al-bent samples, while Table 1 presents the surface area measurements. All of the clay samples exhibit isotherms similar to Type IV, which is characteristic of porous adsorbents with pore sizes between 15 and 100 Å, in accordance with the classification of the International Union of Pure and Applied Chemistry (IUPAC) [40]. The type IV physisorption isotherm is associated with the capillary condensation that takes place in the mesopores. The isotherm exhibits limited uptake over a wide range of P/P_0 and shows monolayer-multilayer adsorption features in the initial part of the curve [41]. The provided classification offers initial details regarding the characteristics of the adsorbent. The morphology of the adsorbent, including its specific pore structures and the degree of compaction, influences the shape and position of the hysteresis loop. Changes in porosity characteristics are suggested by the varying appearances of LDH-coated bentonite. B- Na^+ exhibits a type IV isotherm with a broad H2-type hysteresis loop, which is thought to be linked to ink-bottle-like pores of varying radii. These pores are usually formed by agglomerating or compacting non-uniformly sized and arranged spherical particles [42].

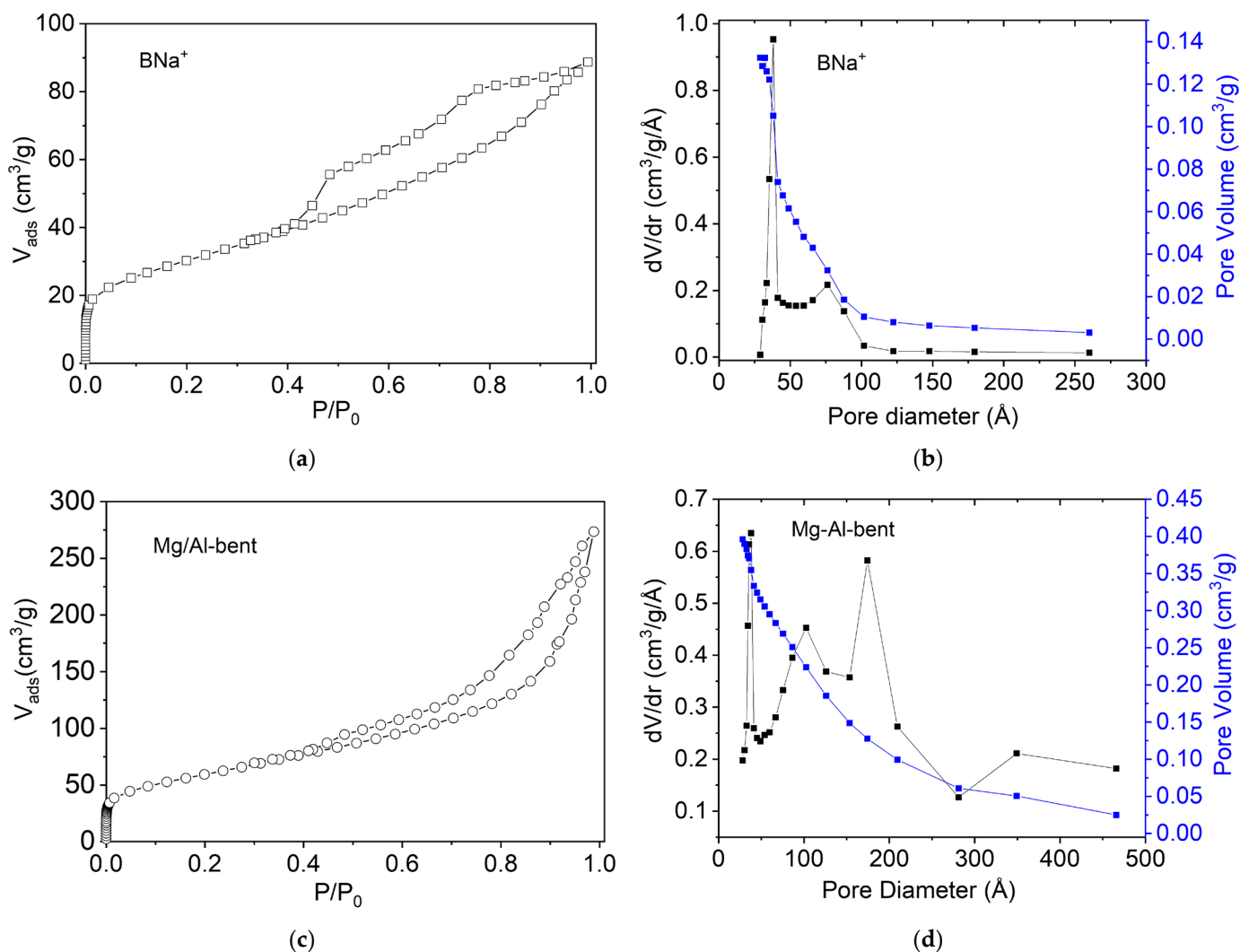


Figure 4. Cont.

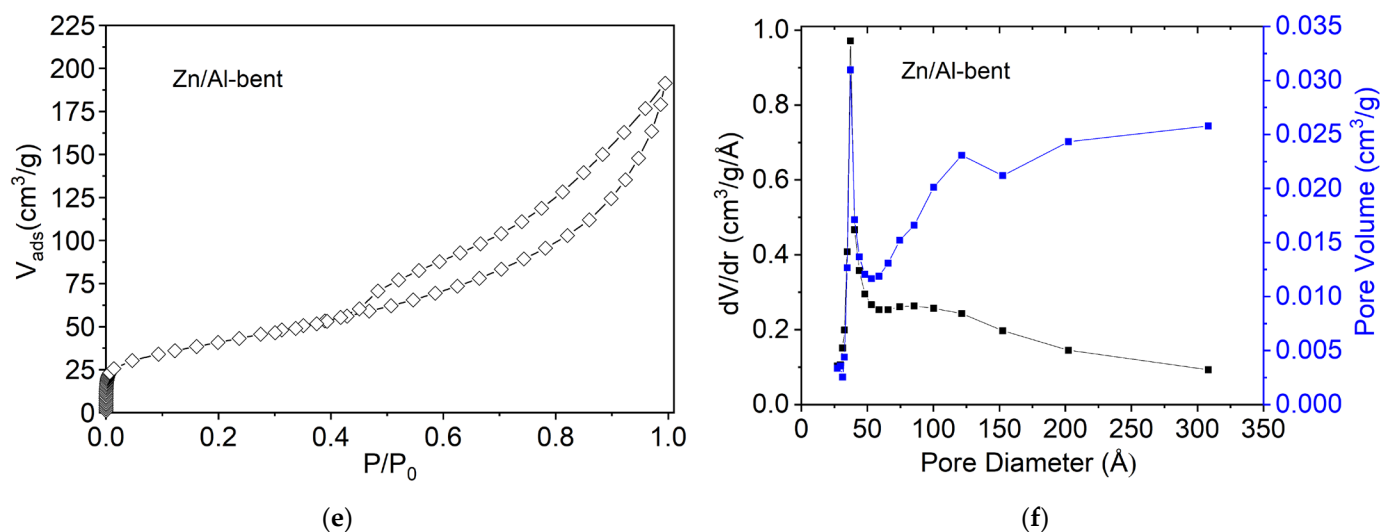


Figure 4. N₂ adsorption–desorption isotherms of (a,b) B-Na⁺, (c,d) Mg/Al-bent, and (e,f) Zn/Al-bent. The corresponding pore size distributions are shown as well for all samples.

Table 1. BET surface area, pore volume, and pore diameter of the original bentonite B-Na⁺, Zn/Al-bent, and Mg/Al-bent composites.

Materials	S_{BET} (m ² /g)	Pore Volume (cm ³ /g)	Pore Diameter (nm)
B-Na ⁺	110.43	0.132	5.145
Zn/Al-bent	175.95	0.313	7.179
Mg/Al-bent	209.25	0.423	8.087

Both Mg/Al-bent and Zn/Al-bent composites exhibit a well-defined H3 hysteresis loop, indicating a system with slit-shaped pores. The adsorption branch is vertical at a relative pressure close to one, and the desorption branch is roughly at medium pressure. The specific surface areas are 110.43 m²/g for B-Na⁺, 175.95 m²/g for Zn/Al-bent, and 209.25 m²/g for Mg/Al-bent. The pore volumes are 0.132 cm³/g for B-Na⁺, 0.313 cm³/g for Zn/Al-bent, and 0.423 cm³/g for Mg/Al-bent.

The results indicate that the specific surface area of the composites is significantly greater than that of the original bentonite. This can be explained by the increase in roughness resulting from the intercalation of LDH or the deposition of nanoparticles, which generates additional mesopores. The modification of the structure and enhancement of the surface chemistry of bentonite by coating can promote adsorption processes. The presence of LDH will increase the porosity and surface area of intercalated bentonite. Table 1 shows that Mg/Al-bent and Zn/Al-bent have higher BET surface areas than B-Na⁺. Other modifications to the textural characteristics of bentonite are evidenced by the average pore diameter and the total pore volume. The coating of LDH on the bentonite matrix causes significant changes in the structural properties of the solid, resulting in an increase in pore volume and surface area. The pore size distribution obtained by the Barrett-Joyner-Halenda method from the desorption curves is shown in Figure 4. A peak radius between 10 Å and 50 Å dominating the mesoporous region is observed in the distribution curves of the samples.

3.1.4. Analysis by Scanning Electron Microscopy

Scanning electron microscopy was utilized to analyze the morphology and microstructure of Mg/Al-bent and Zn/Al-bent composites, along with the B-Na⁺ reference. Figure 5a displays the SEM image of the B-Na⁺ bentonite, which exhibits lamellar aggregates with an irregular, plate-like structure. After modification, the Zn/Al LDH (Figure 5b) and Mg/Al LDH (Figure 5c) particles were bound to the surface of the bentonite. This is supported by

the image showing ultrafine, thin crystal formations that resemble leaves, forming either dense assemblies or a more open honeycombed texture.

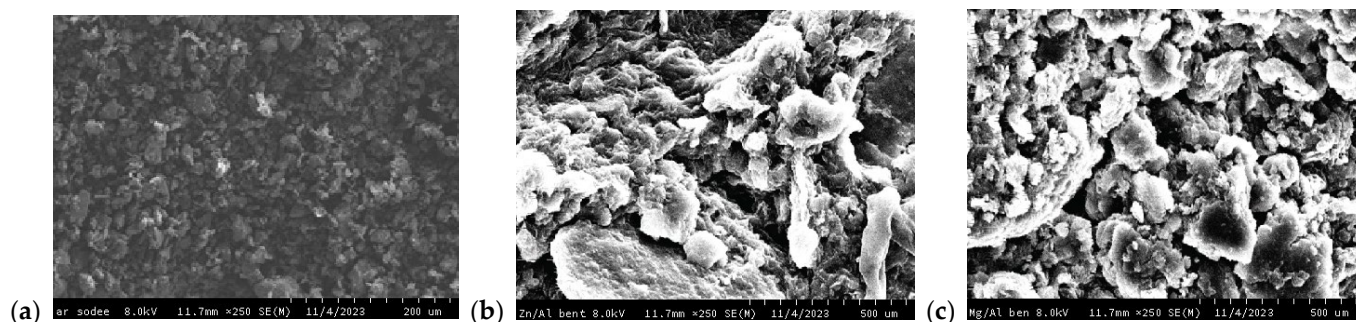


Figure 5. SEM images of (a) B-Na⁺, (b) Zn/Al-bent, and (c) Mg/Al-bent.

3.2. Adsorption of Orange II Dye

The interaction among adsorbent dosage, contact time, and initial dye concentration can be intricate. For example, a higher initial concentration may quickly saturate the active sites of the adsorbent, while an increase in adsorbent dosage could counterbalance this saturation. Contact time could also affect adsorption kinetics, allowing more or less time for dye molecules to bind to adsorption sites. At higher initial concentrations, there may be more competing dye molecules for adsorption sites. This can affect the overall adsorption efficiency. This competition could be mitigated or exacerbated by changes in adsorbent dosage and contact time.

Additionally, the pH of the solution and the temperature can also influence adsorption efficiency. Variations in temperature and pH could alter the chemical interactions between the dye molecules and the surface of the adsorbent, affecting the overall adsorption process.

Although the sequence of experiments was not systematically approached, we meticulously considered the potential interactions between variables and interpreted the results with these factors in mind. Regarding pH, it was selected to work at a pH of 7, which is close to the natural pH of the dye. Furthermore, under acidic conditions, the metal hydroxides of the composites dissolve, while in an alkaline environment, the concentration of competitive hydroxyl ions (OH⁻) may increase [43].

In aqueous solutions, the Orange II dye exists in various forms [44]. However, at pH 2 to 9, only partial ionization (HL⁻) is present, while at pH > 12, full ionization is predominant [45].

3.2.1. Effect of Contact Time

Based on our earlier observations, it appears that the bentonite does not have a significant adsorption capacity for Orange II. The reason for that is the negative charged layers in its structure that cause an electrostatic repulsive effect on the anionic Orange II molecules [46]. However, when modified with LDH, the adsorption of Orange II is significantly enhanced. Figure 6 illustrates the adsorption data of Orange II versus contact time. Experiments were conducted at a constant temperature of 25 °C and pH 7, using an adsorbent dosage of 4 g/L and an initial dye concentration of 3.4 g/L. The plots depict the adsorption of Orange II on Zn/Al-bent and Mg/Al-bent, revealing three distinct phases: instantaneous adsorption in the first hours, progressive equilibrium in the second phase, and a phase of ultimate equilibrium. At first, the composites Mg/Al-bent and Zn/Al-bent had many unoccupied active surface sites. However, over time, the number of available sites decreases. The adsorption of Orange II on Mg/Al-bent is particularly fast, achieving complete adsorption within 3 h with an initial efficiency of 85% of the maximum capacity (724.20 mg/g). Similar rapid kinetics were observed for Orange II on the Zn/Al-bent composite. The dye was fully saturated after 5 h, resulting in a removal rate of 74%, which corresponds to an adsorption capacity of 630.08 mg/g. The control experiments yielded

results indicating that the contaminant concentration remained stable regardless of contact time, suggesting a significant lack of adsorption in the absence of LDH composites.

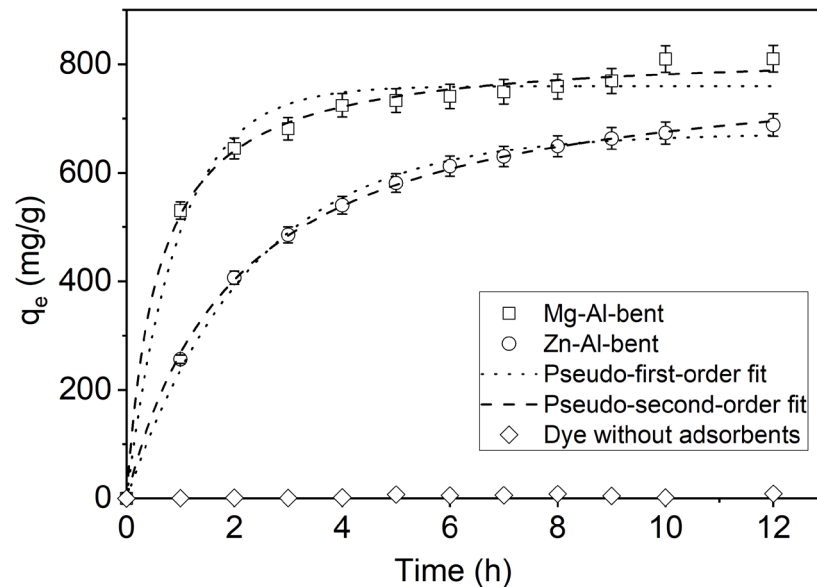


Figure 6. Fit of pseudo-first-order and pseudo-second-order kinetic models for the adsorption of Orange II on Mg-Al-bent and Zn-Al-bent (C_0 of dye = 3.4 g/L; adsorbent concentration = 0.4 g/100 mL; pH = 7; $T = 25$ °C). Control experiments were conducted without the use of adsorbents.

The adsorption kinetics were modelled using the pseudo-first-order [47] and pseudo-second-order [48] approaches. The equations are as follows:

$$q_t = q_e \left(1 - e^{-k_1 t}\right) \quad (3)$$

$$q_t = \frac{k_2 q_e^2 t}{1 + k_2 q_e t} \quad (4)$$

The variables q_e and q_t represent the dye adsorption amount (mg/g) at equilibrium and at time t (min), respectively. The constants k_1 (min^{-1}) and k_2 ($\text{g}/(\text{mg min})$) denote the pseudo-first-order and pseudo-second-order rates of adsorption, respectively.

The experimental isotherm data were simulated using the standard Origin[®] software (version Pro 9.0). The most relevant model(s) for understanding the Orange II adsorption process onto the composite were chosen. Based on the results presented in Table 2, the R_1^2 values were relatively low, ranging between 0.978 and 0.995. The results indicate that the adsorption of Orange II does not follow a controlled diffusion process. It does not fit the pseudo-first-order equation proposed by Lagergren [47]. To determine the order of adsorption kinetics of Orange II by the composites, the pseudo-second-order model is a suitable method. This is supported by the correlation coefficient R_2^2 , which ranges between 0.995 and 0.999.

Table 2. Kinetic constants for pseudo-first-order and pseudo-second-order models for Orange II on Mg/Al-bent and Zn/Al-bent composites.

Adsorbants	q_e (exp) (mg/g)	Pseudo-First-Order Model			Pseudo-Second-Order Model		
		k_1 (min^{-1})	q_e (cal) (mg/g)	R_1^2	k_2 (g/mg min)	q_e (cal) (mg/g)	R_2^2
Zn/Al-bent	630.08	0.433	672.61	0.995	0.490	813.11	0.999
Mg/Al-bent	724.20	1.045	759.61	0.978	1.715	826.84	0.995

Both models were evaluated by statistical analysis across several criteria, including sum of squares, mean square, reduced chi-square, and residual sum of squares. Upon examining the trends in these metrics, it became apparent that the pseudo-second-order model exhibited generally superior performance compared to the pseudo-first-order model (Table 3). Likewise, based on the q_e values cited in Table 2, it is noted that the values calculated by the pseudo-second-order model ($q_e = 813.11$ and 826.84 mg/g) significantly exceed those determined experimentally ($q_e = 630.08$ and 724.20 m/g) for Zn/Al-bent and Mg/Al-bent, respectively.

Table 3. Anova results for pseudo-first-order and pseudo-second-order models (see Table 2). SS: sum of squares; MS: mean square; Ψ^2 : reduced chi-square; RSS: residual sum of squares.

Adsorbants	Pseudo-First-Order Model				Pseudo-Second-Order Model			
	SS	MS	Ψ^2	RSS	SS	MS	Ψ^2	RSS
Zn/Al-bent	3.654	1.827	1.787×10^{-4}	0.001	3.656	1.828	2.363×10^{-5}	2.363×10^{-4}
Mg/Al-bent	5.802	2.901	0.001	0.010	5.811	2.905	2.103×10^{-4}	0.002

The experimental kinetic data were compared with the results of the pseudo-second-order model fit. The results showed a small difference, with a coefficient of variation of 1%, between the theoretical and experimental values. This result provides further evidence for the suitability of the pseudo-second-order model in describing the kinetics of dye adsorption by the composites [49].

These results confirm previous studies [50,51] that found the adsorption kinetics of dyes on clay supports follow a pseudo-second-order model. The phenomenon is explained by the fact that instead of occupying one adsorption site on the solid surface, adsorbate molecules may occupy two, resulting in a dual behavior. Table 2 shows that the rate constants for Zn/Al-bentonite and Mg/Al-bentonite were 0.490 and 1.715 g/(mg min), respectively. The results indicate that Mg/Al-bentonite has a higher affinity for the dye due to its higher adsorption capacity and faster kinetics towards Orange II compared to Zn/Al-bentonite. This suggests that Orange II reacts more strongly with certain active sites on the Mg/Al-bent surface than with other sites on the Zn/Al-bent surface, possibly due to the involvement of the mesoporous structure, which allows for better diffusion of the dye molecule.

3.2.2. Effect of Adsorbent Concentration

In order to determine the optimal amount of Mg/Al-bent and Zn/Al-bent composites to be added to the dye solution, a series of experiments were conducted using 100 mL of a 1 g/L dye solution, with varying amounts of Mg/Al-bent or Zn/Al-bent introduced. Figure 7 shows the effect of the adsorbent dose on removing Orange II from the aqueous solution.

It is noteworthy that Mg/Al-bent exhibits superior color reduction yields compared to Zn/Al-bent. The amount of dye adsorbed by Mg/Al-bent increases as the adsorbent is added, up to a mass of 4 g. After this point, the decolorization yield plateaus. For Zn/Al-bent, the maximum removal is achieved at a dosage of 6 g/L, with a negligible increase in percentage removal thereafter. To illustrate these observations, the results for several distinct adsorbent concentrations (2, 4, 6, 8, and 10 g/L) will be compared. The adsorption capacity increases significantly, from 260.26 g/g (57.8%) for Zn/Al-bent to 316.00 g/g (70.22%) for Mg/Al-bent at 2 g/L of adsorbent; from 136.31 g/g (60.58%) for Zn/Al-bent to 224.74 g/g (99.88%) for Mg/Al-bent at 4 g/L of adsorbent; from 93.06 g/g (62.04%) for Zn/Al-bent to 149.85 g/g (99.90%) for Mg/Al-bent at 6 g/L of adsorbent; from 75.07 g/g (66.72%) for Zn/Al-bent to 112.43 g/g (99.93%) for Mg/Al-bent at 8 g/L of adsorbent; and from 67.03 g/g (74.48%) for Zn/Al-bent to 89.92 g/g (99.92%) for Mg/Al-bent at 10 g/L of adsorbent.

The increase in adsorption sites with the mass of the adsorbent is responsible for this behavior, which reaches a saturation point in the decolorization process [52]. The initial dye

concentration remains constant in this scenario. The addition of more clay mass to the solution results in an expanded transfer surface and an enhanced adsorption rate. It has been confirmed that LDH-coated bentonite can remove dyes even at higher initial concentrations, which suggests its potential applicability in real-world wastewater treatment.

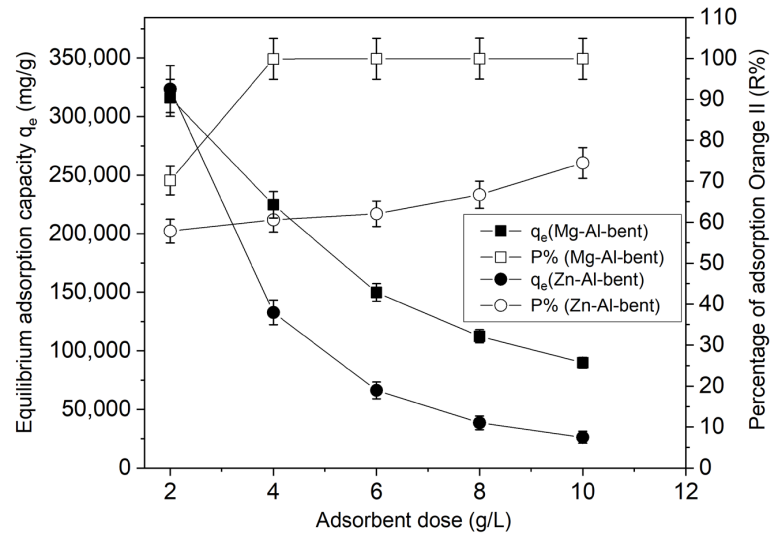


Figure 7. The impact of adsorbent dosage on the removal efficiency R (%) and equilibrium adsorption capacity q_e of Orange II was investigated under experimental conditions of $\text{pH} = 7$, $C_o = 1 \text{ g/L}$, $T = 25 \text{ }^\circ\text{C}$, and contact time $t = 6 \text{ h}$.

3.2.3. Adsorption Isotherms

Adsorptive isotherms are plotted as a ratio of dye adsorbed per unit mass of compound (q_e) to the equilibrium concentration (C_e) of dye in solution at a fixed temperature [53], elucidating the equilibrium interactions between Mg/Al-bent and Zn/Al-bent composites with Orange II. Both composites exhibit impressive adsorption capacities for Orange II, as shown in Figure 8. During the adsorption process, the concentration gradient facilitates the absorption of dye molecules by Mg/Al-bent and Zn/Al-bent composites. The adsorption isotherm shows that Mg/Al-bent absorbs the largest quantity of dye.

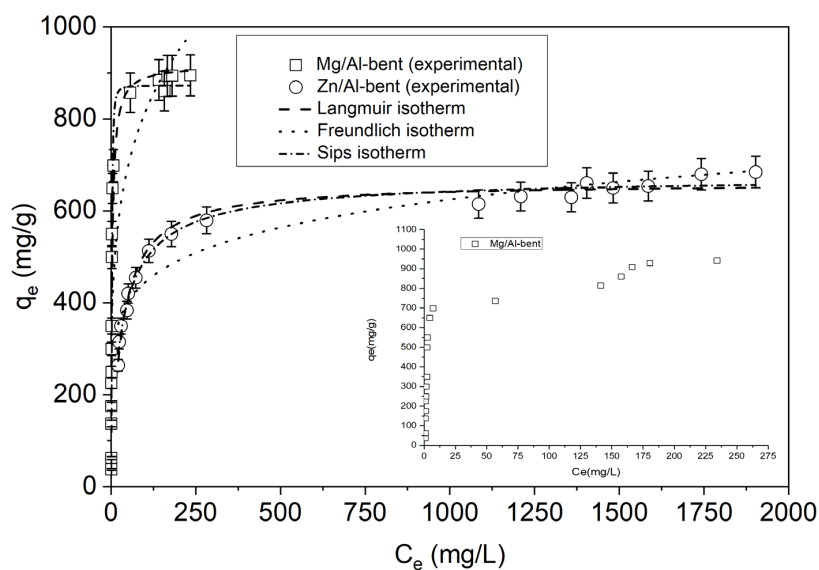


Figure 8. Adsorption isotherms for the removal of Orange II on Mg/Al-bent (\square) and Zn/Al-bent (\circ) were used under the following experimental conditions: adsorbent concentration = 0.1 g/25 mL ; contact time $t = 6 \text{ h}$; $\text{pH} = 7$; and $T = 25 \text{ }^\circ\text{C}$.

Within the concentration range of 150–4000 mg/L, Zn/Al-bentonite and Mg/Al-bentonite removed 68% and 99% of the dye, respectively. It is noteworthy that Mg/Al-bentonite has not yet reached saturation, indicating the potential for further adsorption. This is hypothesized to be due to the formation of a monolayer on active surface sites, with additional adsorption occurring on the already adsorbed dye, creating new adsorption sites [18]. The adsorption capacity of Orange II on Zn/Al-bent increases with the initial concentration of dye, ultimately reaching saturation. All isotherms are H-shaped according to the Giles et al. classification, indicating high adsorbate affinity for the adsorbent, resulting in near-complete adsorption in dilute solutions [54]. Following the initial steep rise, the isotherm plateaus, signifying the attainment of adsorption equilibrium. At equilibrium concentration, the dye adsorption on Zn/Al-bent and Mg/Al-bent reaches 650.34 and 892.03 mg/g, respectively. The micropore structure and surface area primarily determine the affinity of Zn/Al-bent and Mg/Al-bent for organic compounds. Mg/Al-bent has a larger S_{BET} of 209.25 m²/g and V_p of 0.423 cm³/g compared to Zn/Al-bent ($S_{\text{BET}} = 175.95$ m²/g and $V_p = 0.313$ cm³/g), while the layered structures follow the same order.

Modeling adsorption equilibria involves mathematically representing the balance between the quantity of pollutant in the liquid phase (C_e) and the quantity of pollutant adsorbed on the material (q_e). This study analyzes the adsorption equilibrium using the commonly employed Freundlich [55] (Equation (5)), Langmuir [56] (Equation (6)), and Sips (Langmuir–Freundlich) [57] (Equation (7)) isotherms for studying adsorption isotherms in adsorbent/adsorbate systems.

$$q_e = k_f C_e^{(1/n)} \quad (5)$$

$$q_e = \frac{k_L q_m}{1 + k_L C_e} C_e \quad (6)$$

$$q_e = \frac{q_{smax} b_s C_e^\beta}{1 + b_s C_e^\beta} \quad (7)$$

The Freundlich constants $1/n$ and k_f are related to the adsorption intensity and adsorption capacity, respectively. The Langmuir constant k_L is related to the affinity of the binding sites (L/mg), while q_{max} represents the monolayer adsorption capacity of the adsorbent. The maximum adsorption capacity, q_{smax} (SIPS), is expressed in mg/g, where b_s is the equilibrium constant for heterogeneous solids. The parameter that represents heterogeneity is denoted as β .

Table 4 and Figure 8 present the outcomes obtained from applying the Langmuir, Freundlich, and Sips models.

Table 4. Langmuir, Freundlich, and Sips nonlinear parameters for Orange II adsorption on Zn/Al-bent and Mg/Al-bent composites.

Isotherms	Parameters	Adsorbents	
		Zn/Al-bent	Mg/Al-bent
Langmuir	$q_{L,max}$ (mg/g)	660.32	917.27
	b_L (L/mg)	0.033	0.311
	R^2	0.980	0.932
Freundlich	k_f (mg/g) ^{1-1/n}	224.77	290.22
	$1/n$	0.147	0.223
	R^2	0.913	0.779
Sips (L-F)	q_{Smax} (mg/g)	678.45	872.41
	b_S (L/mg)	0.059	0.192
	β	0.823	1.903
	R^2	0.983	0.974

The Langmuir and Sips models seem to be appropriate for the adsorption of Orange II on Zn/Al bentonite and Mg/Al bentonite, as indicated by their R^2 values (>0.97). In addition, a statistical analysis was performed on the results obtained from the three models. This analysis considered different criteria, such as sum of squares, mean square, reduced chi-square, and residual sum of squares. Table 5 shows that the Langmuir and Sips models outperformed the Freundlich model. Additionally, the maximum adsorption capacity (q_{\max}) values calculated from the Sips and Langmuir models were consistent with the experimental data, indicating the efficacy of these models in describing the dye adsorption process. The Langmuir model assumes a homogeneous surface, implying that Orange II adsorption on modified bentonite may be treated as a single-layer adsorption with no interactions between adsorbed molecules. The strong interaction between adsorbent and adsorbate [58] indicates that chemisorption is the primary uptake mechanism in the adsorption process of dye molecules. This finding is consistent with the results of kinetic modeling.

Table 5. ANOVA results for Freundlich, Langmuir, and Sips models (see Table 4). SS: sum of squares; MS: mean square; Ψ^2 : reduced chi-square; RSS: residual sum of squares.

Adsorbants	Freundlich				Langmuir				Sips			
	SS	MS	χ^2	RSS	SS	MS	χ^2	RSS	SS	MS	χ^2	RSS
Mg/Al-bent	6.120	3.062	0.023	0.368	6.380	3.190	0.007	0.113	6.453	2.151	0.002	0.039
Zn/Al-bent	5.084	2.542	0.001	0.025	5.103	2.551	3.872×10^{-4}	0.005	5.105	1.701	3.200×10^{-4}	0.004

3.2.4. Effect of Temperature

Analysis of the thermodynamics of the adsorption process is critical in determining the nature and feasibility of a reaction. Thermodynamic parameters, such as standard Gibbs free energy change (ΔG°), standard entropy change (ΔS°), and standard enthalpy change (ΔH°), are used to calculate the adsorption change based on temperature and adsorption procedure [59]. These parameters can be calculated using the following equation:

$$\ln K_0 = -\frac{\Delta H^\circ}{RT} + \frac{\Delta S^\circ}{RT} \quad (8)$$

The molar gas constant, denoted by R , has a value of 8.314 J/(mol K). The absolute temperature is represented by T . To determine the adsorption distribution coefficient (K_0), $\ln(q_e/C_e)$ was plotted against C_e at different temperatures and extrapolated to $C_e = 0$ using the method suggested by Khan and Singh [60]. The free energy of the adsorption process can be determined using the following equations:

$$\begin{pmatrix} \Delta G^\circ = -RT \ln K_0 \\ \Delta G^\circ = \Delta H^\circ - T \Delta S^\circ \end{pmatrix} \quad (9)$$

The literature extensively discusses the temperature effect, which affects the mobility of dye molecules, and the dynamic equilibrium between equilibrium concentration and adsorbed quantity. Previous studies have shown varying results. For example, a study found a significant influence of decreasing temperature on the adsorbed quantity of Basic Yellow 2 (BY2) dye on natural clay, suggesting an exothermic process [61]. However, previous studies have shown that the adsorption of azoic tartrazine dye onto activated carbon derived from apricot stones is an endothermic process [62].

The values for ΔS° and ΔH° were obtained from the intercept of the plot of the natural logarithm of K_0 and the slope versus reciprocal temperature (Figure 9) and are listed in Table 6. The thermodynamic parameters were measured over a temperature range of 283–298 K and 313 K and showed a negative ΔG° value, indicating the feasibility and spontaneous nature of the adsorption on the modified clay. The ΔH° value suggests that the adsorption process is endothermic. The rise in temperature activates the adsorption sites, which is also reflected in the increase in the number of adsorbed molecules or particles.

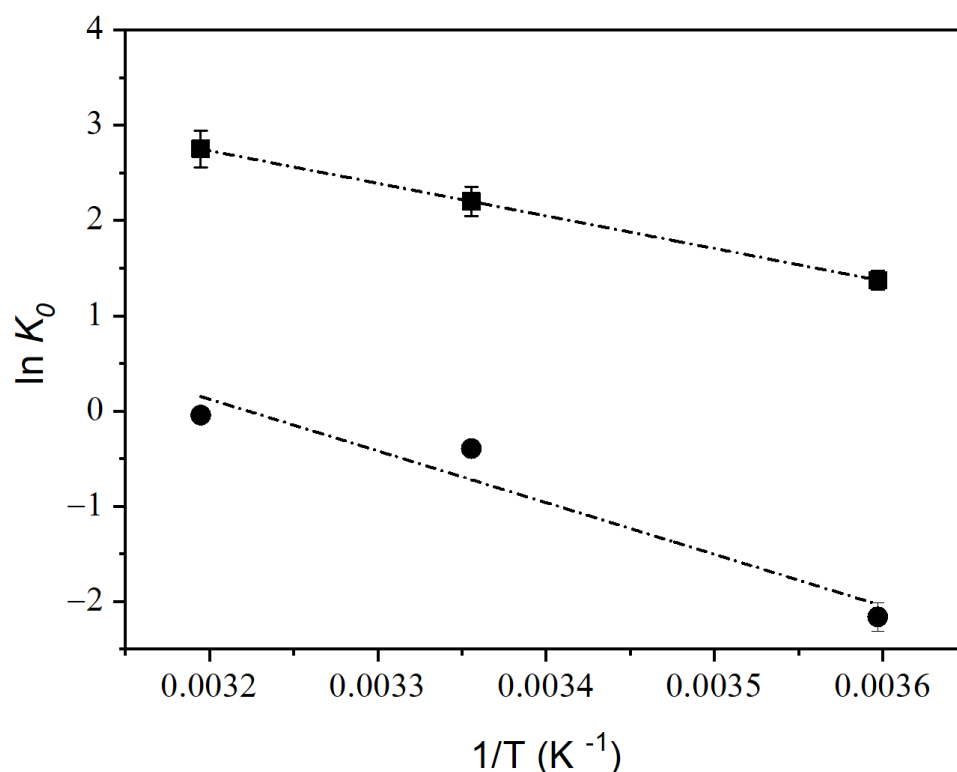


Figure 9. Plots of $\ln K_0$ versus reciprocal temperature were used to evaluate the thermodynamic parameters of Orange II removal on Mg/Al-bent (filled squares) and Zn/Al-bent (filled circles), applying the following experimental conditions: adsorbent concentration = 0.1 g/25 mL; contact time $t = 6$ h; and pH = 7.

Table 6. Thermodynamic parameters for the adsorption of Orange II on Mg/Al-bent and Zn/Al-bent composites.

T (°C)	Adsorbents					
	ΔG^0 (kJ/mol)	Zn/Al-bent ΔH^0 (kJ/mol)	ΔS^0 (J/mol·K)	ΔG^0 (kJ/mol)	Mg/Al-bent ΔH^0 (kJ/mol)	ΔS^0 (J/mol·K)
10	-5.087			-3.230		
25	-0.976	45.125	145.431	-5.450	28.433	113.702
40	-0.115			-7.152		

The positive ΔS^0 values suggest an increase in randomness at the solid solution interface during dye adsorption on the composite. This observation is consistent with previous findings for the adsorption of RB dye on activated carbon [63]. The magnitude of ΔH^0 can be applied to distinguish between chemisorption (80–200 kJ/mol) and physisorption (2.1–20.9 kJ/mol), and the optimized values fall within the range indicative of chemisorption.

4. Discussion

Azoic dyes exist primarily in an anionic form, which causes them to be repelled by the negatively charged surfaces of bentonite. Our aim in the modification process was to incorporate Mg/Al and Zn/Al LDHs into the interlayer space by replacing compensating cations. The objective was to create micro-mesoporous materials while preserving the layered structure. The methodology was supported by X-ray diffraction results, which revealed a two-dimensional network, and by BET isotherm outcomes, which demonstrated an increase in pore volume and specific surface area. Modifying the clay with cationic clays like LDHs makes the clay more hydrophobic towards organic molecules and balances the

bentonite's negative charge with a positive charge, thereby enhancing the adsorption of anionic dyes.

4.1. Adsorption Mechanism

The adsorption mechanism of Orange II onto Mg/Al-bentonite and Zn/Al-bentonite composites operates through two pathways. The adsorption on the external surface takes place by means of electrostatic interactions between the positively charged surface of the composite (after the immobilization of the LDHs) and the negatively charged sulfonic groups of the Orange II molecules (Dye-SO³⁻). This finding indicates a noteworthy contribution to adsorption, consistent with prior research. The difference in adsorption quantity between Mg/Al-bentonite and Zn/Al-bentonite composites is due to variations in porosity, which affect physical adsorption through the pore structure. Furthermore, the adsorption mechanism adheres to the pseudo-second-order kinetic model, suggesting primarily chemical adsorption.

It has been demonstrated that the adsorption process involves primarily chemical adsorption, which includes electrostatic interactions, as well as physical adsorption within the pore structure acting as auxiliary adsorption.

On the basis of the structural characterization of the exhausted materials after the adsorption, it can be concluded that the mechanism of the adsorption of Orange II on the studied materials is related to electrostatic interactions. This conclusion aligns with the results of previous studies on the adsorption of various anionic dyes on comparable adsorbent materials [64–67].

The difference in adsorption quantity between Mg/Al-bentonite and Zn/Al-bentonite composites may be attributed to the dye's affinity and the surface properties of the two composites. According to the proposed mechanism, Orange II could adsorb onto the external surface of the composites and infiltrate the interlayer spaces. The surface that adsorbs became more positive after immobilizing the LDHs. This facilitated the adsorption of the anionic dye through electrostatic interactions. The correlation coefficients of the pseudo-first-order kinetic model were lower than those of the pseudo-second-order model. This suggests that the adsorption of Orange II onto Mg/Al-bent and Zn/Al-bent was chemical in nature. Increasing the dosage of modified clays resulted in increased adsorption, allowing more adsorbate molecules to form chemical bonds with the adsorbent surface. The thermodynamic parameters suggest that the adsorption of Orange II onto Mg/Al-bent and Zn/Al-bent is both spontaneous and endothermic. The experimental data fit well with the Sips and Langmuir isotherm models. This indicates a monolayer adsorption phenomenon. However, the experimental data did not fit well with the Freundlich isotherm model.

4.2. Comparison of the Adsorption Capacities with the Literature

To demonstrate the effectiveness of low-cost composites for Orange II adsorption, a comparison of the adsorption capacity of this material with that of other low-cost adsorbents is essential. Table 7 shows a comparative analysis of the adsorption capacities of the developed compounds for Orange II and other adsorbents described in the literature. The results highlight the superior adsorption capabilities of coated bentonite for the removal of this pollutant.

Table 7. A comparison was made between the adsorption capacities obtained from Langmuir isotherms of Mg/Al-bentonite and Zn/Al-bentonite adsorbents for Orange II dye and those of various adsorbents described in the literature.

Adsorbents	q_e (mg·g ⁻¹) Taken from Langmuir Isotherm	Studied Concentrations	Ref.
Polyethylene glycol-modified LDH	724.64	$C_0 = 200\text{--}800$ mg·L ⁻¹ $T = 50$ °C pH = 6.7	[68]
Cationic polymer-bentonite poly([2-(methacryloyloxy)ethyl] trimethylammonium chloride), (PMETAC)-modified bentonite (Bent-PMETAC).	208.6	$C_0 = 50\text{--}500$ mg·L ⁻¹ $T = 25$ °C Natural pH	[69]
Activated carbon fiber, ACFT	230	$C_0 = 30\text{--}80$ mg·L ⁻¹ $T = 30$ °C	[70]
ACFC (CARBOFLEX, Anshan East Asia Carbon Fibers)	1260	Natural pH	
Zn ₂ Al-layered double hydroxide, LDH-R	36.9	$C_0 = 40\text{--}200$ mg·L ⁻¹ $T = 20$ °C pH = 6.3	[71]
Zn ₂ Al-layered double hydroxide, LDH-W	42.5		
Iron-benzenetricarboxylate (Fe(BTC))	435	$C_0 = 10\text{--}250$ mg·L ⁻¹ $T = 25$ °C pH = 7	[66]
Mg/Al-bentonite	917.27	Present study	
Zn/Al-bentonite	660.32	Present study	

5. Conclusions

The literature has not extensively explored the synthesis of bentonite-modified LDH and its surface functionalization. However, these cost-effective composites show promise as an alternative to conventional methods for removing azo dyes from water. In this study, we utilized a low-cost approach by using bentonite, a material abundant in Algeria. Mg/Al-bentonite and Zn/Al-bentonite adsorbents are highly effective for treating effluent due to their high specific surface area, large pore volume, predominantly microporous pore size distribution, rapid adsorption kinetics, and high adsorption capacity. These materials are particularly suitable for adsorbing organic pollutants, including anionic dyes.

This study focuses on the adsorption of the anionic dye Orange II onto composites based on bentonite modified with LDHs. The results show remarkable adsorption efficiency, particularly at higher concentrations and shorter equilibrium times. The experimental data fit well with a pseudo-second-order kinetic model, and the equilibrium data agree well with Langmuir and Sips isotherms. The adsorption of Orange II follows a chemical sorption process. The monolayer adsorption capacities for Zn/Al-bent and Mg/Al-bent are 660.32 and 917.27 mg/g, respectively. The thermodynamic calculations of the adsorption data indicate that the adsorption of Orange II onto Zn/Al-bent and Mg/Al-bent occurs spontaneously and is of an endothermic nature.

Author Contributions: Conceptualization, U.M.; methodology, K.B. and U.M.; investigation, M.M.B. and A.A.-A.; formal analysis, A.A.-A. and K.B.; data curation, M.M.B., A.A.-A. and K.B.; writing—original draft preparation, U.M.; writing—review and editing, U.M.; visualization, K.B. and U.M.; supervision, U.M.; project administration, U.M. All authors have read and agreed to the published version of the manuscript.

Funding: This research received no external funding.

Data Availability Statement: Data are contained within the article.

Acknowledgments: This work is the result of close collaboration between the two laboratories, i.e., LPCMCE of USTOMB and UMET of the University of Lille. The authors gratefully acknowledge the support from MDPI, the Algerian Ministry of Higher Education and Scientific Research (MESRS), the

General Directorate of Scientific Research and Technological Development (DGRSDT) of Algeria, the University of Sciences and Technology of Oran (USTOMB)/Algeria, the French Ministry of Higher Education and Research (MENESR), the CNRS, and the University and the CROUS of Lille/France.

Conflicts of Interest: The authors declare no conflicts of interest.

References

1. Tripathi, M.; Singh, S.; Pathak, S.; Kasaudhan, J.; Mishra, A.; Bala, S.; Garg, D.; Singh, R.; Singh, P.; Singh, P.K.; et al. Recent Strategies for the Remediation of Textile Dyes from Wastewater: A Systematic Review. *Toxics* **2023**, *11*, 940. [\[CrossRef\]](#) [\[PubMed\]](#)
2. Moharrery, L.; Otadi, M.; Miraly, N.; Rezaei Zangeneh, M.M.; Amiri, R. Degradation of toluidine red, an oil soluble azo dye by *Halomonas* strain IP8 at alkaline condition. *Chem. Eng. Commun.* **2019**, *206*, 61–68. [\[CrossRef\]](#)
3. Alam, R.; Mahmood, R.A.; Islam, S.; Ardiati, F.C.; Solihat, N.N.; Alam, M.B.; Lee, S.H.; Yanto, D.H.Y.; Kim, S. Understanding the biodegradation pathways of azo dyes by immobilized white-rot fungus, *Trametes hirsuta* D7, using UPLC-PDA-FTICR MS supported by in silico simulations and toxicity assessment. *Chemosphere* **2023**, *313*, 137505. [\[CrossRef\]](#) [\[PubMed\]](#)
4. Amini, B.; Otadi, M.; Partovinia, A. Statistical modeling and optimization of Toluidine Red biodegradation in a synthetic wastewater using *Halomonas* strain Gb. *J. Environ. Health Sci. Engineer.* **2019**, *17*, 319–330. [\[CrossRef\]](#) [\[PubMed\]](#)
5. Jing, W.; Zhigang, Z.; Lei, H.; Zhaoguo, Q.; Qibin, X.; Shenghao, Z.; Xian, T.; Dechang, Z. Effective removal of Orange II dye by porous Fe-base amorphous/Cu bimetallic composite. *Colloids Surf. A Physicochem. Eng. Asp.* **2023**, *656*, 130388.
6. Signorelli, S.C.M.; Costa, J.M.; de Almeida Neto, A.F. Electrocoagulation-flotation for orange II dye removal: Kinetics, costs, and process variables effects. *J. Environ. Chem. Eng.* **2021**, *9*, 106157. [\[CrossRef\]](#)
7. Thoa, L.K.; Thao, T.P.; Nguyen-Thi, M.; Nguyen, D.C.; Wei Ooi, C.; Park, S.; Lan, T.T.; Quang, H.T.; Khoo, K.S.; Show, P.L.; et al. Microbial biodegradation of recalcitrant synthetic dyes from textile-enriched wastewater by *Fusarium oxysporum*. *Chemosphere* **2023**, *325*, 138392. [\[CrossRef\]](#) [\[PubMed\]](#)
8. Kamali, M.; Ebrahimi, A.; Vatanpour, V. New dithiocarbamate-based polymer (DTCP) as an additive to improve microporous polysulfone membrane efficiency in lead and dye removal. *J. Environ. Manag.* **2023**, *339*, 117925. [\[CrossRef\]](#) [\[PubMed\]](#)
9. Ahmed, M.; Mashkoo, F.; Nasar, A. Development, Characterization, and Utilization of Magnetized Orange Peel Waste as a Novel Adsorbent for the Confiscation of Crystal Violet Dye from Aqueous Solution. *Groundw. Sustain. Dev.* **2020**, *10*, 100322. [\[CrossRef\]](#)
10. Maleš, L.; Fakin, D.; Bračić, M.; Gorgieva, S. Efficiency of Differently Processed Membranes Based on Cellulose as Cationic Dye Adsorbents. *Nanomaterials* **2020**, *10*, 642. [\[CrossRef\]](#)
11. Pham, T.D.; Bui, V.P.; Pham, T.N.; Le, T.M.D.; Nguyen, K.T.; Bui, V.H.; Nguyen, T.D. Adsorptive Removal of Anionic Azo Dye New Coccine Using Silica and Silica-Gel with Surface Modification by Polycation. *Polymers* **2021**, *13*, 1536. [\[CrossRef\]](#) [\[PubMed\]](#)
12. Mansouri, F.E.; Farissi, H.E.; Zerrouk, M.H.; Cacciola, F.; Bakkali, C.; Brigui, J.; Lovillo, M.P.; Esteves da Silva, J.C.G. Dye Removal from Colored Textile Wastewater Using Seeds and Biochar of Barley (*Hordeum vulgare* L.). *Appl. Sci.* **2021**, *11*, 5125. [\[CrossRef\]](#)
13. Benedettia, V.; Patuzzia, F.; Baratieri, M. Gasification char as a potential substitute of activated carbon in adsorption applications. *Energy Procedia* **2017**, *105*, 712–717. [\[CrossRef\]](#)
14. Dong, Y.; Lin, H.; Zhao, Y.; Menzembere, E.R.G.Y. Remediation of vanadium-contaminated soils by the combination of natural clay mineral and humic acid. *J. Clean. Prod.* **2021**, *279*, 123874. [\[CrossRef\]](#)
15. Doodoo, D.; Appiah, G.; Acquah, G.; Junior, T. Fixed-bed column study for the remediation of the bauxite-liquid residue using acid-activated clays and natural clays. *Heliyon* **2023**, *9*, 14310. [\[CrossRef\]](#) [\[PubMed\]](#)
16. Jawad, A.H.; Saber, S.E.M.; Abdulhameed, A.S.; Farhan, A.M.; AlOthman, Z.A.; Wilson, L. Characterization and applicability of the natural Iraqi bentonite clay for toxic cationic dye removal: Adsorption kinetic and isotherm study. *J. King Saud Univ. Sci.* **2023**, *35*, 102630. [\[CrossRef\]](#)
17. Belbachir, I.; Makhoukhi, B. Adsorption of Bezathren dyes onto sodic bentonite from aqueous solutions. *J. Taiwan Inst. Chem. Eng.* **2017**, *75*, 105–111. [\[CrossRef\]](#)
18. Bouberka, Z.; Kacha, S.; Kameche, M.; Elmaleh, S.; Derriche, Z. Sorption study of an acid dye from an aqueous solution using modified clays. *J. Hazard. Mater.* **2005**, *119*, 117–124. [\[CrossRef\]](#)
19. Tahir, S.S.; Rauf, N. Removal of a cationic dye from aqueous solutions by adsorption onto bentonite clay. *Chemosphere* **2006**, *63*, 1842–1848. [\[CrossRef\]](#)
20. Souza, P.R.; Dotto, G.L.; Salau, N.P.G. Experimental and mathematical modeling of hindered diffusion effect of cationic dye in the adsorption onto bentonite. *J. Environ. Chem. Eng.* **2019**, *7*, 102891. [\[CrossRef\]](#)
21. Araújo, M.E.B.; Silva, V.C.; Fernandes, J.V.; Cartaxo, J.M.; Rodrigues, A.M.; Menezes, R.R.; Neves, G. Innovative adsorbents based on bentonite mining waste for removal of cationic dyes from wastewater. *Environ. Sci. Pollut. Res.* **2022**, *29*, 90446–90462. [\[CrossRef\]](#) [\[PubMed\]](#)
22. Hao, Y.; Yan, L.; Yu, H.; Yang, K.; Yu, S.; Shan, R.; Du, B. Comparative study on adsorption of basic and acid dyes by hydroxy-aluminum pillared bentonite. *J. Mol. Liq.* **2014**, *199*, 202–207. [\[CrossRef\]](#)
23. Chinoune, K.; Bentaleb, K.; Bouberka, Z.; Nadim, A.; Maschke, U. Adsorption of reactive dyes from aqueous solution by dirty bentonite. *Appl. Clay Sci.* **2016**, *123*, 64–75. [\[CrossRef\]](#)
24. Desai, H.; Kannan, A.; Sai Kumar, G. Reddy Sustainable and rapid pillared clay synthesis with applications in removal of anionic and cationic dyes. *Microporous Mesoporous Mater* **2023**, *352*, 112488. [\[CrossRef\]](#)

25. Majiya, H.; Clegg, F.; Sammon, C. Bentonite-Chitosan composites or beads for lead (Pb) adsorption: Design, preparation, and characterisation. *Appl. Clay Sci.* **2023**, *246*, 107180. [[CrossRef](#)]
26. Zhong, H.; Guan, Y.; Qiu, Z.; Grady, B.P.; Su, J.; Huang, W. Application of carbon coated bentonite composite as an ultra-high temperature filtration reducer in water-based drilling fluid. *J. Mol. Liq.* **2023**, *375*, 121360. [[CrossRef](#)]
27. Ahmed, M.A.; Dania, K.A. Bentonite-layered double hydroxide composite as potential adsorbent for removal of Abamectin pesticide from wastewater. *Results Surf. Interfaces* **2023**, *10*, 100099.
28. Bouhent, M.M.; Derriche, Z.; Denoyel, R.; Prevot, V.; Forano, C. Thermodynamical and structural insights of orange II adsorption by Mg_RAlNO₃. *J. Solid State Chem.* **2011**, *184*, 1016–1024. [[CrossRef](#)]
29. Forano, C.; Hibino, T.; Leroux, F.; Taviot-Guého, C. Chapter 13.1 Layered Double Hydroxides. In *Developments in Clay Science*; Bergaya, F., Theng, B.K.G., Lagaly, G., Eds.; Elsevier: Amsterdam, The Netherlands, 2006; Volume 1, pp. 1021–1095.
30. Mu'azu, N.D.; Jarrah, N.; Kazeem, T.S.; Zubair, M.; Al-Harthi, M. Bentonite-layered double hydroxide composite for enhanced aqueous adsorption of Eriochrome Black T. *Appl. Clay Sci.* **2018**, *161*, 23–34. [[CrossRef](#)]
31. Hu, Q.; Xu, Z.; Qiao, S.; Haghseresht, F.; Wilson, M.; Lu, G.Q. A novel color removal adsorbent from heterocoagulation of cationic and anionic clays. *J. Colloid Interface Sci.* **2007**, *308*, 191–199. [[CrossRef](#)]
32. Bouberka, Z.; Khenifi, A.; Sekrane, F.; Bettahar, N.; Derriche, Z. Adsorption of Direct Red 2 on bentonite modified by cetyltrimethylammoniumbromide. *Chem. Eng. J.* **2008**, *136*, 295–305.
33. Bouberka, Z.; Khenifi, A.; Ait Mahamed, H.; Haddou, B.; Belkaid, N.; Bettahar, N.; Derriche, Z. Adsorption of Supranol Yellow 4 GL from aqueous solution by surfactant-treated aluminum/chromium-intercalated bentonite. *J. Hazard. Mater.* **2009**, *162*, 378–385. [[CrossRef](#)] [[PubMed](#)]
34. Sisnayati, S.M.; Aprianti, N.; Komala, R.; Dwipayana, H.; Faizal, M. Metal Pillared Bentonite Synthesis and Its Characteristics Using X-Ray Diffraction. *J. Ecol. Eng.* **2022**, *23*, 68–74. [[CrossRef](#)]
35. Kaur, M.; Ubhi, M.K.; Grewal, J.K.; Singh, D. Insight into the structural, optical, adsorptive, and photocatalytic properties of MgFe₂O₄-bentonite nanocomposites. *J. Phys. Chem. Solids* **2021**, *154*, 111060. [[CrossRef](#)]
36. Zhang, Y.; Liu, Q.; Wu, Z.; Zhang, Y. Thermal behavior analysis of two bentonite samples selected from China. *J. Therm. Anal. Calorim.* **2015**, *121*, 1287–1295. [[CrossRef](#)]
37. Utami, H.P.; Siburian, D.M. Organometallic [Fe₃O(OOCC₆H₅)₆(H₂O)₃](NO₃) as intercalant of bentonite. *Sci. Technol. Indones.* **2016**, *1*, 20–24. [[CrossRef](#)]
38. Oussalah, A.; Boukerroui, A.; Aichour, A.; Djellouli, B. Cationic and anionic dyes removal by low-cost hybrid alginate/natural bentonite composite beads: Adsorption and reusability studies. *Int. J. Biol. Macromol.* **2019**, *124*, 854–862. [[CrossRef](#)]
39. Botti, S.; Almaguila, S.; Cantarini, L.; Palucci, A.; Puiu, A.; Rufoloni, A. Trace level detection and identification of nitro-based explosives by surface-enhanced Raman spectroscopy. *J. Raman Spectrosc.* **2013**, *44*, 463–468. [[CrossRef](#)]
40. Guo, W.; Hu, Z.; Zhang, X.; Yu, R.; Wang, L. Shale gas adsorption and desorption characteristics and its effects on shale permeability. *Energ. Explor. Exploit.* **2017**, *35*, 463–481. [[CrossRef](#)]
41. Touaa, N.D.; Bouberka, Z.; Gherdaoui, C.; Supiot, P.; Roussel, P.; Pierlot, C.; Maschke, U. Titanium and iron-modified delaminated muscovite as photocatalyst for enhanced degradation of Tetrabromobisphenol A by visible light. *Funct. Mater. Lett.* **2020**, *13*, 2051008. [[CrossRef](#)]
42. Adelkhani, H.; Ghaemi, M.; Ruzbehani, M. Evaluation of the Porosity and the Nano-structure Morphology of MnO₂ Prepared by Pulse Current Electrodeposition. *Int. J. Electrochem. Sci.* **2011**, *6*, 123–135. [[CrossRef](#)]
43. Mandal, S.; Mayadevi, S.; Kulkarni, B.D. Adsorption of aqueous Selenite [Se(IV)] Species on Synthetic Layered Double Hydroxide Materials. *Ind. Eng. Chem. Res.* **2009**, *48*, 7893–7898. [[CrossRef](#)]
44. Bourikas, K.; Styliad, M.; Kondarides, D.I.; Verykios, X.E. Adsorption of acid orange 7 on the surface of titanium dioxide. *Langmuir* **2005**, *21*, 9222–9230. [[CrossRef](#)]
45. Zaheer, Z.; Bawazir, W.A.; Al-Bukhari, S.M.; Basaleh, A.S. Adsorption, equilibrium isotherm, and thermodynamic studies to the removal of acid orange 7. *Mater. Chem. Phys.* **2019**, *232*, 109–120. [[CrossRef](#)]
46. Sharma, P.; Borah, D.J.; Das, P.; Das, M.R. Cationic and anionic dye removal from aqueous solution using montmorillonite clay: Evaluation of adsorption parameters and mechanism. *Desalin. Water Treat.* **2016**, *57*, 8372–8388. [[CrossRef](#)]
47. Lagergren, S. Zur Theorie der sogenannten Adsorption geloster Stoffe. *K. Sven. Vetenskapsakademiens Handl.* **1898**, *24*, 1–39.
48. Ho, Y.S.; McKay, G. Kinetic model for lead (II) sorption onto peat. *Adsorpt. Sci. Technol.* **1998**, *16*, 243–255. [[CrossRef](#)]
49. Ho, Y.S.; McKay, G. The kinetics of sorption of divalent metal ions onto sphagnum moss peat. *Water Res.* **2000**, *34*, 735–742. [[CrossRef](#)]
50. Tian, Y.; Ma, H.; Xing, B. Preparation of surfactant modified magnetic expanded graphite composites and its adsorption properties for ionic dyes. *Appl. Surf. Sci.* **2021**, *537*, 147995. [[CrossRef](#)]
51. Belbel, A.; Kharroubi, M.; Janot, J.M.; Abdessamad, M.; Haouzi, A.; Lefkaier, I.K.; Balme, S. Preparation and characterization of homoionic montmorillonite modified with ionic liquid: Application in dye adsorption. *Colloids Surf. A Physicochem. Eng. Asp.* **2018**, *558*, 219–227. [[CrossRef](#)]
52. Doğan, M.; Karaoğlu, M.H.; Alkan, M. Adsorption kinetics of maxilon yellow 4GL and maxilon red GRL dyes on kaolinite. *J. Hazard. Mater.* **2009**, *165*, 1142–1151. [[CrossRef](#)]

53. Bolis, V. Fundamentals in Adsorption at the Solid-Gas Interface. Concepts and Thermodynamics. In *Calorimetry and Thermal Methods in Catalysis*; Springer Series in Materials Science; Springer: Berlin/Heidelberg, Germany, 2013; Volume 154, Chapter 1; pp. 1–50.
54. Giles, C.H.; Huitson, A. A general treatment and classification of the solute adsorption isotherms. *J. Colloid Interface Sci.* **1974**, *47*, 755–777. [[CrossRef](#)]
55. Freundlich, H.M.F. Über die Adsorption in Lösungen. *Z. Phys. Chem.* **1906**, *57*, 385–470. [[CrossRef](#)]
56. Langmuir, I. The constitution and fundamental properties of solids and liquids. Part I. solids. *J. Am. Chem. Soc.* **1916**, *38*, 2221–2295. [[CrossRef](#)]
57. Jeppu, G.P.; Clement, T.P. A modified Langmuir–Freundlich isotherm model for simulating pH-dependent adsorption effects. *J. Contam. Hydrol.* **2012**, *129–130*, 46–53. [[CrossRef](#)] [[PubMed](#)]
58. Rusmin, R.; Sarkar, B.; Liu, Y.; McClure, S.; Naidu, R. Structural evolution of chitosan-palygorskite composites and removal of aqueous lead by composite beads. *Appl. Surf. Sci.* **2015**, *353*, 363–375. [[CrossRef](#)]
59. Kausar, A.; Iqbal, M.; Javed, A.; Aftab, K.; Nazli, Z.; Bhatti, H.N.; Nouren, S. Dyes adsorption using clay and modified clay: A review. *J. Mol. Liq.* **2018**, *256*, 395–407. [[CrossRef](#)]
60. Khan, A.A.; Singh, R.P. Adsorption thermodynamics of carbofuran on Sn(IV) arsenosilicate in H⁺, Na⁺ and Ca²⁺ forms. *J. Colloid. Sci.* **1987**, *24*, 33–42. [[CrossRef](#)]
61. Öztürk, A.; Malkoc, E. Adsorptive potential of cationic Basic Yellow 2 (BY2) dye onto natural untreated clay (NUC) from aqueous phase: Mass transfer analysis, kinetic and equilibrium profile. *Appl. Surf. Sci.* **2014**, *299*, 105–115. [[CrossRef](#)]
62. Albroomi, H.I.; Elsayed, M.A.; Baraka, A.; Abdelmaged, M.A. Batch and fixed-bed adsorption of tartrazine azo-dye onto activated carbon prepared from apricot stones. *Appl. Water Sci.* **2017**, *7*, 2063–2074. [[CrossRef](#)]
63. Al-degs, Y.; Khraisheh, M.A.M.; Allen, S.J.; Ahmad, M.N. Effect of carbon surface chemistry on the removal of reactive dyes from textile effluent. *Wat. Res.* **2000**, *34*, 927–935. [[CrossRef](#)]
64. Geraud, E.; Bouhent, M.; Derriche, Z.; Leroux, F.; Prevot, V.; Forano, C. Texture effect of layered double hydroxides on chemisorption of orange II. *J. Phys. Chem. Solids* **2007**, *68*, 818–823. [[CrossRef](#)]
65. Khosla, E.; Kaur, S.; Dave, P.N. Mechanistic study of adsorption of acid orange-7 over aluminum oxide nanoparticles. *J. Eng.* **2013**, *2013*, 593534. [[CrossRef](#)]
66. García, E.; Medina, R.; Lozano, M.; Hernández Pérez, I.; Valero, M.; Franco, A. Adsorption of azo-dye orange II from aqueous solutions using a metal-organic framework material: Iron-benzenetricarboxylate. *Materials* **2014**, *7*, 8037–8057. [[CrossRef](#)] [[PubMed](#)]
67. Jin, X.; Yu, B.; Chen, Z.; Arocena, J.M.; Thring, R.W. Adsorption of orange II dye in aqueous solution onto surfactant-coated zeolite: Characterization, kinetic, and thermodynamic studies. *J. Colloid Interf. Sci.* **2014**, *435*, 15–20. [[CrossRef](#)] [[PubMed](#)]
68. Mandal, S.; Kalaivanan, S.; Mandal, A.B. Polyethylene glycol-modified layered double hydroxides: Synthesis, characterization and study on adsorption characteristics for removal of acid orange II from aqueous solution. *ACS Omega* **2019**, *4*, 3745–3754. [[CrossRef](#)]
69. Wang, L.; Meng, F.; Pei, M.; Guo, W.; Liu, G.; Du, S. Synthesis of a cationic polymer-bentonite composite utilizing a simple and green process for the adsorption of acid orange 7 from aqueous solution. *J. Macromol. Sci. B* **2019**, *58*, 794–809. [[CrossRef](#)]
70. Chiang, H.-M.; Chen, T.-C.; Pan, S.-D.; Chiang, H.-L. Adsorption characteristics of Orange II and Chrysophenine on sludge adsorbent and activated carbon fibers. *J. Hazard. Mater.* **2009**, *161*, 1384–1390.
71. Tâmaş, A.; Cozma, I.; Coheci, L.; Lupa, L.; Rusu, G. Adsorption of Orange II onto Zn₂Al-Layered Double Hydroxide Prepared From Zinc Ash. *Front. Chem.* **2020**, *8*, 573535. [[CrossRef](#)]

Disclaimer/Publisher’s Note: The statements, opinions and data contained in all publications are solely those of the individual author(s) and contributor(s) and not of MDPI and/or the editor(s). MDPI and/or the editor(s) disclaim responsibility for any injury to people or property resulting from any ideas, methods, instructions or products referred to in the content.